www.sciencemag.org/cgi/content/full/science.1243289/DC1

Supplementary Materials for

Deterministically Encoding Quantum Information Using 100-Photon Schrödinger Cat States

Brian Vlastakis,* Gerhard Kirchmair, Zaki Leghtas, Simon E. Nigg, Luigi Frunzio, S. M. Girvin, Mazyar Mirrahimi, M. H. Devoret, R. J. Schoelkopf

*Corresponding author. E-mail: brian.vlastakis@yale.edu

Published 26 September 2013 on *Science* Express
DOI: 10.1126/science.1243289

This PDF file includes:

Materials and Methods
Supplementary Text
Figs. S1 to S10
Tables S1 and S2
References

Supplementary Material: Deterministically encoding quantum information using 100-photon Schrödinger cat states

Brian Vlastakis,[1] Gerhard Kirchmair,[1] Zaki Leghtas,[1,2] Simon E. Nigg,[1] Luigi Frunzio,[1] S. M. Girvin,[1] Mazyar Mirrahimi,[1,2] M. H. Devoret,[1] and R. J. Schoelkopf[1]

[1]*Departments of Physics and Applied Physics, Yale University, New Haven, CT 06511, USA*
[2]*INRIA Paris-Rocquencourt, Domaine de Voluceau, B.P. 105, 78153 Le Chesnay Cedex, France*

(Dated: September 24, 2013)

MATERIALS AND METHODS

Qubit fabrication

The transmon qubit (made of a single Josephson junction galvanically connected with two stripline antennas) is fabricated on a single-crystal C-plane sapphire substrate using Dolan bridge double-angle electron beam deposition lithography. Film thickness for each deposition is approximately 20 nm and 60 nm. Between these depositions, an AlOx barrier was grown via thermal oxidation for 720 seconds in 2000 Pa static pressure of gaseous mixture 85% argon and 15% oxygen. This resulted in a junction normal state resistance of 4.65 kΩ. We use the term 'vertical transmon' (describing the orientation of the electric field with respect to the film plane) to distinguish from the dipole geometry of the standard '3D transmon'.

Measurement setup

The system is probed through input couplers connected to each cavity resonator. These inputs have coupling quality factors, $Q_c \simeq 10^7$ (and thus under-coupled from other losses). The output coupler for the high frequency (readout) resonator is set to a coupling quality factor, $Q_c \simeq 25,000$. This asymmetric coupling allows for transmission detection of qubit-state dependent phase shifts in the readout resonator. Fig. S1 shows a diagram of the measurement setup. Microwave generators produce signals that are transmitted from room temperature to the sample with 20 dB attenuation at 4 K stage, 20 dB attenuation through directional coupler and an additional 10 dB attenuation at base (25 mK). The output signal from the readout resonator travels through two cryogenic isolators to a HEMT amplifier with noise temperature of 5 K at the 4 K stage. At room temperature, this signal is down-converted to 25 MHz where it is finally digitized using a 1GS/s ADC and converted to an integrated digital homodyne voltage.

Hamiltonian parameters

Our system can be described by three modes which all inherit nonlinearity from a single Josephson junction that can be expressed by the Hamiltonian

$$H/\hbar = \sum_i \tilde{\omega}_i a_i^\dagger a_i - E_J(\cos\varphi + \tfrac{1}{2}\varphi^2) \tag{S1}$$

where $\tilde{\omega}_i$ is the linear resonance of the i^{th} coupled mode, E_J is the Josephson energy, and φ is the phase across the Josephson junction. Each coupled mode contributes to junction phase $\varphi = \frac{1}{\phi_0}\sum_i \phi_i(a_i^\dagger + a_i)$ where ϕ_0 is the flux quantum and ϕ_i is the flux coefficient of the i^{th} mode in the basis of the coupled system. Taylor expanding to the sixth order about small excursions in φ and ignoring constant terms in the Hamiltonian produces

$$H/\hbar = \sum_i \tilde{\omega}_i a_i^\dagger a_i - E_J[\frac{1}{24}\varphi^4 - \frac{1}{720}\varphi^6 + \mathcal{O}(\varphi^8)]. \tag{S2}$$

Following the analysis in (33) gives the approximate Hamiltonian:

$$\begin{aligned} H/\hbar \approx & \sum_i \omega_i a_i^\dagger a_i \\ & - \sum_i K_i a_i^{\dagger 2} a_i^2 - \sum_{i\neq j} \chi_{ij} a_i^\dagger a_i a_j^\dagger a_j \\ & + \sum_i K_i' a_i^{\dagger 3} a_i^3 + \sum_{i\neq j} \chi_{ij}' a_i^\dagger a_i a_j^{\dagger 2} a_j^2 \\ & + \chi_{ijk} a_i^\dagger a_i a_j^\dagger a_j a_k^\dagger a_k \end{aligned} \tag{S3}$$

where ω_i are the non-linear single photon resonances of each mode, K_i is the anharmonic term of each mode (also known as the self-Kerr), χ_{ij} is the state dependent shift between modes i and j, K_i' is a non-linear correction to K_i, χ_{ij}' is a non-linear correction to the state dependent shift, and χ_{ijk} is a three-mode state dependent shift. K_i' and χ_{ij}' can be viewed as terms that create photon-number dependence in the K_i and χ_{ij} terms. Measured and estimated values in this experiment can be found in Table SI. The relevant terms for this experiment when restricting the 'qubit' mode to $|g\rangle\langle g|$ and $|e\rangle\langle e|$ states and restricting to terms with interaction strengths greater than transition linewidths give the reduced Hamiltonian

$$\begin{aligned} H/\hbar \approx & \ \omega_q |e\rangle\langle e| + \omega_s a^\dagger a + \omega_r b^\dagger b \\ & - \chi_{qs} a^\dagger a |e\rangle\langle e| - \chi_{qr} b^\dagger b |e\rangle\langle e| \\ & - K_s a^{\dagger 2} a^2 + \chi_{qs}' a^{\dagger 2} a^2 |e\rangle\langle e| \end{aligned} \tag{S4}$$

where $\omega_{q,s,r}$ are the transition frequencies of the qubit, storage, and readout modes; χ_{qs} and χ_{qr} are the state dependent shifts between the qubit and the storage/readout modes; K_s is the storage mode self-Kerr; and χ_{qs}' is the non-linear correction to the state dependent shift. Methods for measuring K_s, and χ_{qs}' are described in future sections. It is interesting to note is that our measured value for the ratio of χ_{qs}'/K_s is greater than one, a feature that cannot be predicted using this Hamiltonian approximation.

Experiment initialization

The experiments shown here rely on the assumption that the qubit/cavity system is initialized in the ground state $|0,g\rangle$. If there exists some probability of initial residual excitation P_e, techniques such as post-selection can be performed to remove these systematic preparation errors. In this experiment, we can realize a similar operation by applying a conditional cavity displacement tone D^e_β on an initial mixed state $\rho = |0\rangle\langle 0| \otimes \{P_g |g\rangle\langle g| + P_e |e\rangle\langle e|\}$ to produce $D^e_\beta \rho D^{e\dagger}_\beta = P_g |0,g\rangle\langle 0,g| + P_e |\beta,e\rangle\langle\beta,e|$. For this experiment, we use a weak tone with a drive strength $\epsilon/2\pi = 990$ kHz and duration 2.5 μs to initialize each experiment which produces an estimated displaced state $|\beta,e\rangle$ where $|\beta| \approx 17$ for any residual qubit excitation. This operation ideally entangles any initial qubit excitation with photons outside of our measurable Hilbert space (for this experiment, our tomography displacements do not exceed $|\alpha| = 6$). This technique runs at a cost of reduced SNR and some residual cavity state excitation. We measure population of the qubit state P_e before and after initialization to be 0.12 and $\leq$0.01 respectively and population of the cavity one photon Fock state P_1 before and after initialization to be 0.003 and 0.02, respectively.

Multi-component cat state generation sequences

As described in the main text, by concatenating the conditional cavity phase shift C_Φ and the conditional qubit rotation $R^0_{\hat{y},\theta}$ we can create complex cavity states that encode quantum information into a superposition of multiple coherent states. Fig. S2 outlines the sequence of operations required in order to produce the cavity states shown in Fig. 4 of the main text. The phase of the conditional qubit rotations $R^0_{\hat{n},\theta}$ will determine the phase of the interference fringes between each coherent state. In this experiment, we left these phases uncalibrated resulting in states with defined yet arbitrarily chosen superposition phases.

SUPPLEMENTARY TEXT

Heisenberg-limited phase estimation using the qcMAP

The protocol (18) which we outline in the main text (also known as the qcMAP) allows for the deterministic creation of cat states. A cat state's increased sensitivity to cavity displacements could be utilized for high precision metrology experiments (19, 20, 34). Linear schemes using a coherent state $|\beta\rangle$ will have a phase resolution $\delta\Phi$ that scales as $\frac{1}{\sqrt{\bar{n}}}$ where $\bar{n} = |\beta|^2$ is the average energy (in photons) of the coherent state. This scaling is known as the quantum-noise limit. Using entanglement (or in this case, a superposition of photons) allows one to surpass this limit and achieve a scaling of $\frac{1}{\bar{n}}$, known as the Heisenberg limit (20).

Shown in Fig. S3 is a proof-of-principle experiment where we use the qcMAP protocol to realize Heisenberg-limited phase resolution. We compare the scaling of a cat state's sensitivity to phase with a coherent state's sensitivity with equivalent mean energy. To do so, we prepare a qubit state in either $|g\rangle$ or $|g\rangle+|e\rangle$ and map to a cavity state to produce either the states $|\beta\rangle$ or $|0\rangle+|\sqrt{2}\beta\rangle$. Notice that both states have a mean energy $\bar{n} = |\beta|^2$. We implement a cavity phase shift Φ (by changing our cavity drive reference frame) before mapping the cavity state back to the qubit state. We will define the phase resolution $\delta\Phi = 1/\frac{\mathrm{d}P_e}{\mathrm{d}\Phi}$ of these states as the inverse of the maximum slope of the detected qubit population P_e with respect to the phase shift Φ. For a coherent state, this gives a phase resolution $\delta\Phi_D = \sqrt{e/\bar{n}}$. A cat state of equivalent mean energy gives a phase resolution (for small angles of Φ) $\delta\Phi_C = 1/\bar{n}$. In reality, the cat state's sensitivity to phase $\delta\Phi_C$ is an approximation at low energies for $\bar{n}\kappa\tau \ll 1$ where κ is the cavity decay rate and τ is a combination of the time for preparation and detection. For larger energies, the cat state's phase resolution will diverge as $\delta\Phi_C = e^{\bar{n}\kappa\tau}/\bar{n}$.

We measure a phase resolution for cat states of mean energy $\bar{n} = 9$, 15.5, and 22.5 photons and compare them to coherent states with mean energies up to 30 photons (Fig. S3) and show phase resolution scaling indicative of the Heisenberg limit.

Qubit state revival using Ramsey interferometry

We utilize the dispersive shift χ_{qs} in order to create a qubit state-dependent phase shift of the cavity state C_Φ where $\Phi = \chi_{qs}t$. Using Ramsey interferometry, we can characterize this operation by observing the precession of the qubit state phase when interacting with a coherent state $|\beta\rangle$. Performing a Ramsey experiment for various times t and an initial state $|\psi(0)\rangle = |\beta,g\rangle$ results in

$$\begin{aligned}|\psi(t)\rangle &= R_{\hat{y},\frac{\pi}{2}} C_{\Phi=\chi_{qs}t} R_{\hat{y},\frac{\pi}{2}} |\beta,g\rangle \\ &= e^{\frac{\pi}{4}(|e\rangle\langle g| - |g\rangle\langle e|)} e^{-i\chi_{qs}t a^\dagger a |e\rangle\langle e|} e^{\frac{\pi}{4}(|e\rangle\langle g| - |g\rangle\langle e|)} |\beta,g\rangle \\ &= \frac{1}{2}\{(|\beta\rangle - |\beta e^{-i\chi_{qs}t}\rangle)\otimes|g\rangle + (|\beta\rangle + |\beta e^{-i\chi_{qs}t}\rangle)\otimes|e\rangle\}\end{aligned}$$

where $R_{\hat{y},\frac{\pi}{2}}$ is a $\pi/2$ rotation about the y-axis of the qubit Bloch sphere. This results in a qubit excited state probability P_e as

$$\begin{aligned}P_e &= \frac{1}{2}\{1 + \mathrm{Re}(\langle\beta|\beta e^{i\chi_{qs}t}\rangle)\} \\ &= \frac{1}{2}\{1 + e^{|\beta|^2(\cos(\chi_{qs}t)-1)}\cos(|\beta|^2\sin(\chi_{qs}t))\}. \qquad \text{(S5)}\end{aligned}$$

While this relation appears to yield an apparent decay in coherence proportional to $e^{-\frac{1}{2}(|\beta|\chi_{qs}t)^2}$, in actuality this is a coherent precession of the qubit phase dependent on the cavity state. From this, we should also expect to see a revival in the qubit state coherence at a time $t_{\text{revival}} = 2\pi/\chi_{qs}$. Shown in Fig. S4 is this Ramsey experiment for displacements D_β with $|\beta| = 0$ to 2.5 and wait times $t = 0$ to 1 μs. This time-dependent method shows a revival time of 422 ns confirming spectroscopy measurements of the state-dependent shift $\chi_{qs} = 2.36$ MHz. The overall

reduction in revival visibility is due to internal qubit dephasing. Cavity photon decay will also begin to dominate at larger displacements. A shift in the revival time occurs due to higher order interactions in the dispersive Hamiltonian (see later section). This experiment also reveals our precision for a selected cavity phase, $\Delta\Phi = \chi_{qs}\Delta t = 0.015$ radians.

Measuring each step of the qcMAP protocol

The Q-function of a cavity state is $Q(\alpha) = \frac{1}{\pi}\langle\alpha|\rho|\alpha\rangle$ where ρ is the cavity state density matrix and can be a useful tool for detecting the population and phase of a cavity state. With qubit rotations conditioned on the zero-photon Fock state, the Q-function can be measured through qubit/cavity entanglement (16). The operation relies on the assumption that the qubit is in the ground state $|g\rangle$. If the qubit state is unknown, we can perform tomography of the Q-function conditional on the qubit state using various conditional qubit operations. With rotations $R^0_{\hat{y},\pi}$ and $R^0_{\hat{y},\frac{\pi}{2}}$, we can measure conditional Q-functions $Q(\alpha)_{|g\rangle}$, $Q(\alpha)_{|e\rangle}$, and $Q(\alpha)_{|g\rangle+|e\rangle}$ which we use here to illustrate qubit/cavity correlations. Fig. S5 shows each step in the qcMAP protocol beginning with the state, $|\psi\rangle = \frac{1}{\sqrt{2}}\{|0\rangle \otimes (|g\rangle + |e\rangle)\}$ and mapping to the state, $|\psi\rangle = \mathcal{N}\{(|\beta\rangle + |-\beta\rangle) \otimes |g\rangle\}$ where $|\beta| = \sqrt{7}$ and $\mathcal{N} \approx \frac{1}{\sqrt{2}}$.

Cavity state Analysis

Direct Wigner tomography, while being an efficient method for determining the entire cavity state, can also be used for local measurements of the cavity phase space. This could allow for just a small number of measurements to estimate a particular cavity state observable, bypassing the need for full cavity state reconstruction (35). Using the high-resolution Wigner measurements of Fig. 2 in the main text, we compare our ability to calculate observables from both a cavity state reconstruction using linear regression and direct methods using the Wigner function as a quasi-probability distribution.

Cavity state reconstruction

The Wigner function is related to the cavity density matrix by the combination of displacement operators D_α and photon number parity P as

$$W(\alpha) = \frac{2}{\pi}\,\mathrm{Tr}[D^\dagger_\alpha \rho D_\alpha P] \tag{S6}$$

where ρ is the cavity state density matrix. This can be rearranged into a linear equation by

$$\begin{aligned} W(\alpha) &= \frac{2}{\pi}\,\mathrm{Tr}[D_\alpha P D^\dagger_\alpha \rho] \\ &= \mathrm{Tr}[M(\alpha)\rho] \\ &= \sum_{i,j} M_{ji}(\alpha)\rho_{ij} \end{aligned}$$

where $M(\alpha) = D_\alpha P D^\dagger_\alpha$ such that $M_{ji}(\alpha)$ and ρ_{ij} are elements in matrices $M(\alpha)$ and ρ. This linear relation can be inverted using least squares regression to determine each element of ρ_{ij} from $W(\alpha)$. This regression is performed under the constraint that ρ is normalized ($\mathrm{Tr}[\rho] = 1$), positive semi-definite, and truncated at 20 photons. See Fig. S6 for a comparison between the measured and reconstructed Wigner function of the cat state reported in Fig. 2 of the main text.

Calculating observables from cavity state Wigner function

Knowledge of the cavity state density matrix ρ allows for the calculation of the cavity state observable $O(a^\dagger, a)$ by the relation

$$\langle O(a^\dagger, a)\rangle = \mathrm{Tr}[O(a^\dagger, a)\rho]. \tag{S7}$$

This relationship also allows us to calculate the fidelity of the cavity state to a particular pure target state $|\psi_{\mathrm{targ}}\rangle$ by

$$F = \langle\psi_{\mathrm{t}}|\rho|\psi_{\mathrm{t}}\rangle = \mathrm{Tr}[|\psi_{\mathrm{targ}}\rangle\langle\psi_{\mathrm{targ}}|\,\rho].$$

The Wigner function $W(\alpha^*, \alpha)$ (which we now denote as a function of a complex value α and its complex conjugate α^*) holds an equivalent method for calculating mean observables

$$\big\langle O(a^\dagger, a)\big\rangle = \frac{1}{\pi}\int o(\alpha^*, \alpha) W(\alpha^*, \alpha)\mathrm{d}^2\alpha \tag{S8}$$

where the $o(\alpha^*, \alpha)$ is the complex function corresponding to the operator, $O(a^\dagger, a)$. This function has the relation (36, 37) with any symmetrically ordered $O(a^\dagger, a)$ as

$$\{O(a^{\dagger m}, a^n)\}_s \rightarrow o(\alpha^*, \alpha) = \alpha^{*m}\alpha^n$$

where m, n are integers and $\{..\}_s$ denotes symmetric ordering of $a^\dagger$ and a. Using this relationship and commutation relations, the expectation value of any observable can be inferred. Fidelity of a pure target state can also be calculated in this way following

$$F = \langle\psi_{\mathrm{t}}|\rho|\psi_{\mathrm{t}}\rangle = \frac{1}{\pi}\int W_{\mathrm{targ}}(\alpha^*, \alpha) W(\alpha^*, \alpha)\mathrm{d}^2\alpha$$

where $W_{\mathrm{targ}}(\alpha^*, \alpha)$ is the target state Wigner function. No least-squares fitting and density matrix reconstruction is necessary to retrieve these mean observables though some error will occur due to discrete integration. Table SII shows the inferred expectation values of photon number $a^\dagger a$, position $\frac{1}{2}(a^\dagger + a)$, momentum $\frac{1}{2i}(a^\dagger - a)$, and fidelity to a target state $|\psi_{\mathrm{targ}}\rangle$ of the measured cat state in Fig. 2 of the main text using these two different methods.

Qubit/cavity state mapping and mapping back

Since qubit to cavity state mapping is deterministic, we can reverse the process in order to map an encoded cavity state back to the qubit. We explore this feature by performing a 'map/map-back' experiment to diagnose sources of error in the mapping operation. This will also allow us to isolate errors between cavity state preparation and Wigner tomography.

We perform quantum process tomography on the map/map-back operation acting on the qubit. The process matrix (see Fig. S7) for each cat state size reveals that a dominant error in this ideally identity operation is qubit phase coherence. These errors are those most sensitive to photon loss of the cavity state during the mapping process and can be observed in the increased phase errors in the process matrix for map/map-back of cat states with large photon numbers.

Using a Ramsey experiment on the qubit, we can also observe the recovered quantum coherence for mapping a cat state to the cavity then back to the qubit. We perform this experiment for cat states of estimated size: 16, 28, 40, and 100 photons. The reduction in Ramsey contrast with larger cat state sizes is indicative of decoherence due to photon decay during the map/map-back process. This suggests that cat state preparation fidelity could actually be above 0.9 for sizes up 40 photons and above 0.75 for a state of size 100 photons where fidelity F is estimated from contrast C as $F \approx (1+\sqrt{C})/2$. Note that further loss of fidelity not included in this approximation can occur due to effects such as the cavity self-Kerr.

Detecting the cavity state and scaling displacement amplitude

We can perform two varieties of cavity state tomography by utilizing qubit/cavity entangling operations, C_Φ and $R^n_{\hat{n},\theta}$, with cavity displacements D_α. With measurements of zero-photon number probability $P_0(\alpha)$ and mean photon number parity $\langle P(\alpha)\rangle$, we are able to measure cuts of the cavity Q-function and Wigner function, $P_0(\alpha) = \pi Q(\alpha)$ and $\langle P(\alpha)\rangle = \frac{\pi}{2} W(\alpha)$. By performing these tomography measurements on a known state, the cavity vacuum state, we can calibrate our displacement drive strength and normalize our readout signal (see Fig. S8).

A displaced cavity vacuum state will create a photon number probability distribution P_n

$$P_n(\alpha) = |\langle n| D_\alpha |0\rangle|^2 = e^{-|\alpha|^2} \frac{|\alpha|^{2n}}{n!}. \tag{S9}$$

We observe that our readout signal follows this same distribution which we use to calibrate our readout signal and scale our displacement amplitude. We also follow a similar scheme when measuring the mean photon parity $\langle P\rangle = e^{i\pi a^\dagger a}$ of a displaced vacuum state

$$\langle P(\alpha)\rangle = \mathrm{Tr}[P D_\alpha |0\rangle\langle 0| D_\alpha^\dagger] = e^{-2|\alpha|^2}. \tag{S10}$$

From this, we see the expected Gaussian envelope associated with Wigner function of the cavity vacuum state which we can also use to calibrate our displacement amplitude. One must be careful though when calibrating with $\langle P(\alpha)\rangle$, as a thermal state will follow this same envelope and may incorrectly skew displacement calibration. We measure a cavity population $P_1 = 0.02$ in this experiment which gives a small systematic error in displacement calibration, $\delta\alpha/\alpha \approx 0.02$.

Detecting higher-order nonlinear terms

Before attempting to access higher photon Fock states of the cavity Hilbert space, we must ensure that higher order terms in our dispersive approximation will not begin to dominate. For our Hamiltonian, we measure the storage cavity self-Kerr K_s and the non-linearity of the dispersive shift χ'_{qs} to determine whether these interactions are sufficiently weak in comparison to dispersive shift χ_{qs}.

Characterizing storage cavity self-Kerr

A coherent state, $|\beta\rangle$, evolving under a Hamiltonian, $H/\hbar = \omega_s a^\dagger a - K_s a^{\dagger 2} a^2$ experiences a phase precession $\Phi \approx K_s(|\beta|^2 - 1)t$ where t is a waiting time. We measure the cavity Q function of an initially prepared coherent state $|\beta\rangle$ to observe its phase precession and spreading due to the Kerr effect which allows us a time resolved method to determine the cavity self-Kerr (See Fig. S9). This results in a ratio K_s/χ_{qs} of 0.0014 giving a cavity self-Kerr $\frac{K_s}{2\pi} = 3.61$ kHz.

Characterizing non-linearity of the dispersive interaction

According to the expansion of the dispersive Hamiltonian (see section, 'Hamiltonian parameters'), the dispersive shift $\chi_{qs} a^\dagger a |e\rangle\langle e|$ will contain a small non-linear dependence on photon number, $\chi'_{qs} a^{\dagger 2} a^2 |e\rangle\langle e|$. This becomes more obvious at higher photon numbers n when $n\chi'_{qs}$ becomes comparable to χ_{qs}. Performing the Ramsey interferometer experiment shown in Fig. S10, we can observe the qubit state revival with higher mean photon numbers, up to $\bar{n} = 25$ photons . To first order, the non-linearity in the dispersive shift will result in a small change in the qubit state revival time $t_{\mathrm{revival}} = \frac{2\pi}{\chi_{qs} - |\beta|^2 \chi'_{qs}}$. We use this measurement as a time-resolved method to compare χ_{qs} to χ'_{qs} resulting in a ratio $\chi'_{qs}/\chi_{qs} = 0.0018$ giving a nonlinear shift $\chi'_{qs} = 4.2$ kHz.

Conditional/unconditional drives in the strong-dispersive regime

In this experiment, we use fixed frequency interactions and qubit/cavity drives in order to generate and manipulate

entanglement. We can perform both conditional and unconditional qubit/cavity operations by controlling the duration and shape of the driving fields used. The following sections will describe how we can achieve these operations and estimate their limitations.

Conditional qubit rotations

Due to the state-dependent shift between qubit and storage cavity χ_{qs}, the qubit transition frequency is dependent on photon number which we can represent as $\omega_q^n = \omega_q - \chi_{qs} n$ where n is the number of photons in the storage cavity. The idea behind the conditional qubit rotation is to perform a drive that is selective on only one of these transitions in order to entangle the qubit and cavity states. This can only follow exactly for a qubit pulse of infinite duration. Fortunately, we can still realize this operation approximately for pulse durations much greater than $1/\chi_{qs}$.

Using Eq. 1 of the main text, we can introduce a classical drive on resonance with the m^{th} photon number split peak ω_q^m resulting in the Hamiltonian (using the interaction picture)

$$H/\hbar = -\chi_{qs}(a^\dagger a - m)\left|e\right\rangle\left\langle e\right| + \epsilon(t)\sigma_y \tag{S11}$$

where $\epsilon(t)$ is a time-dependent real value representing the amplitude envelope of the microwave drive (we will ignore the phase of the drive) and σ_y is the Pauli spin operator about the y-axis of the Bloch sphere. We can represent this Hamiltonian in a block diagonal form

$$\begin{aligned} H/\hbar &= \sum_n H_n/\hbar \left|n\right\rangle\left\langle n\right| \\ &= \sum_n \{-\chi_{qs}(n-m)\left|e\right\rangle\left\langle e\right| + \epsilon(t)\sigma_y\}\left|n\right\rangle\left\langle n\right|. \end{aligned} \tag{S12}$$

Taking each block, we can transform into a rotating frame

$$\tilde{H}_n/\hbar = \sum_n \epsilon(t) e^{i\Delta_{n,m}t\left|e\right\rangle\left\langle e\right|}\sigma_y e^{-i\Delta_{n,m}t\left|e\right\rangle\left\langle e\right|} \tag{S13}$$

where $\Delta_{n,m} = \omega_q^n - \omega_q^m$. We can predict the evolution of a qubit cavity state $\left|\psi(t)\right\rangle$ by the time-dependent Schrödinger relation

$$\left|\dot{\psi}_n(t)\right\rangle = -\frac{i}{\hbar}\tilde{H}_n(t)\left|\psi_n(t)\right\rangle. \tag{S14}$$

For a state containing exactly m photons, this evolution will produce a qubit rotation $R_{\hat{y},\theta} = e^{i\frac{\theta}{2}\sigma_y}$ where $\theta = 2\int\epsilon(t)\mathrm{d}t$. We can approximate this interaction for all other photon number states $\left|\psi_{n\neq m}(t)\right\rangle$ by looking at the first order Dyson expansion

$$\left|\psi_n(t)\right\rangle \approx \left\{1 - \frac{i}{\hbar}\int^t \mathrm{d}s\tilde{H}_n(s)\right\}\left|\psi_n(0)\right\rangle. \tag{S15}$$

For an initial state $\left|\psi(0)\right\rangle = \sum_{n\neq m} C_n\left|g,n\right\rangle$, this produces

$$\begin{aligned} \left|\psi(t)\right\rangle &\approx \sum_{n\neq m} C_n\{\left|g,n\right\rangle - \frac{i}{\hbar}\int_0^t \mathrm{d}s\tilde{H}_n(s)\left|g,n\right\rangle\} \\ &= \sum_{n\neq m} C_n\{\left|g,n\right\rangle \\ &\qquad - i\int_0^t \mathrm{d}s\epsilon(s)e^{i\Delta_{n,m}s\left|e\right\rangle\left\langle e\right|}\sigma_y e^{-i\Delta_{n,m}s\left|e\right\rangle\left\langle e\right|}\left|g,n\right\rangle\} \\ &= \sum_{n\neq m} C_n\{\left|g,n\right\rangle - \int_0^t \mathrm{d}s\epsilon(s)e^{i\Delta_{n,m}s}\left|e,n\right\rangle\} \\ &\approx \sum_{n\neq m} C_n\{\left|g,n\right\rangle - \hat{\epsilon}\{\Delta_{n,m}\}\left|e,n\right\rangle\} \end{aligned} \tag{S16}$$

where $\hat{\epsilon}\{\omega = \Delta_{n,m}\}$ is the Fourier transform of the drive amplitude envelope $\epsilon(t)$ at a frequency Δ_n. This produces a normalized final state at a time τ as

$$\left|\psi(\tau)\right\rangle = \frac{1}{\sqrt{1+\hat{\epsilon}\{\Delta_n\}^2}}\sum_{n\neq m} C_n\{\left|g,n\right\rangle - \hat{\epsilon}\{\Delta_n\}\left|e,n\right\rangle\}$$

This allows us to put an estimate on the amount of undesired qubit population produced when performing a selective qubit rotation. We will define the 'selectivity' of the qubit drive by its ability to leave all other occupied cavity states $\left|\psi\right\rangle = \sum_{n\neq m} C_n\left|g,n\right\rangle$ in the qubit ground state. This gives the relation for selectivity

$$\mathcal{S} = \left|\left\langle n,g\right|\left.\psi(\tau)\right\rangle\right|^2 = \sum_{n\neq m}\frac{\left|C_n\right|^2}{1+\hat{\epsilon}[\Delta_{n,m}]^2} \tag{S17}$$

For example, when we wish to perform a conditional qubit rotation on the m^{th} photon number split peak, we use a shaped qubit pulse $\epsilon(t) = Ae^{-\sigma_\omega^2 t^2/2}$ where σ_ω is the spectral width of the qubit pulse and $A = \sqrt{8/\pi}\sigma_\omega$ is the amplitude of the drive required to perform a qubit π rotation on the ω_q^m transition. We use $\sigma_\omega = 800$ kHz such that we have a selectivity between the m^{th} level and the $(m\pm1)^{\text{th}}$ level as $\mathcal{S} = (1+\frac{\pi}{8}e^{-\chi_{qs}^2/\sigma_\omega^2})^{-1} > 0.99$. This results in an approximate qubit/cavity entangling operation similar to Eq. 1 in the main text

$$R_{\hat{y},\pi}^m = \left|m\right\rangle\left\langle m\right| \otimes R_{\hat{y},\pi} + \sum_{n\neq m} e^{i\xi_n}\left|n\right\rangle\left\langle n\right| \otimes \mathbb{1} \tag{S18}$$

where $\left|m\right\rangle$ is the selected m^{th} photon Fock state and ξ_n is an induced photon-dependent phase accumulation on all other Fock states.

For this experiment we actually have a looser restriction on the spectral width σ_ω of our selective qubit pulse. In the qubit/cavity mapping sequence (creating a superposition of coherent states, $\left|\beta\right\rangle$ and $\left|-\beta\right\rangle$), we wish to perform the operation $R_{\hat{y},\pi}^0(\left|2\beta,g\right\rangle + \left|0,e\right\rangle) = (\left|2\beta\right\rangle + \left|0\right\rangle)\otimes\left|g\right\rangle$. This requires a qubit π rotation on the $\left|0\right\rangle$ cavity state while being selective against all other occupied Fock states $\left|n\right\rangle$ in the state $\left|2\beta\right\rangle = \sum_{n=0}^\infty C_n\left|n\right\rangle = e^{-\frac{|2\beta|^2}{2}}\sum_{n=0}^\infty\frac{(2\beta)^n}{\sqrt{n!}}\left|n\right\rangle$. For this experiment, we choose a Gaussian-shaped pulse with $\sigma_\omega = 4|\beta|^2\chi_{qs}/5$ which gives a selectivity between

the zero photon Fock state and the displaced cavity state $|2\beta\rangle$ as $\mathcal{S} = \sum_{n=1}^{\infty} |C_n|^2 (1 + \frac{\pi}{8} e^{-(n\chi_{qs})^2/\sigma_\omega^2})^{-1} > 0.99$ for the creation of a cat state of size $S = 4|\beta|^2 > 5$ photons. We create cat states with S =19, 32, 38, and 111 photons using σ_ω = 7.6 MHz, 13.3 MHz, 17.7 MHz, and 39.8 MHz respectively.

For this operation, we can approximate the form of the induced photon-dependent phase accumulation ξ_n. For transitions with large detunings from the drive frequency $\Delta_n = \chi_{qs} n \gg \sigma_\omega$, the accumulated phase ξ_n will follow the AC stark relationship for slowly varying drive envelopes, $\xi_n = \int \epsilon(t)^2 \mathrm{d}t/\Delta_n$. When $1/(2|\beta|) \ll 1$, each Fock state $|n\rangle$ will result an approximate phase $\xi_n \propto 1 - n/(8|\beta|^2)$. This affects the cavity state in two ways: the photon independent term will result in a shift in phase for the coherent state superposition, this can be calibrated by adjusting the relative phase of the drive ϵ; the photon-dependent term will result in a shift of the coherent state which can be calibrated by adjusting the relative phase of the experiment's rotating frame. Taking these calibrations into account, we can approximately achieve the ideal description of the conditional qubit rotation described in Eq. 3 of the main text.

Unconditional qubit rotations

When performing direct Wigner tomography, we must be able to perform qubit rotations independent of the cavity state. In this experiment the qubit and cavity are coupled at all times with a dispersive interaction $\chi_{qs} a^\dagger a \, |e\rangle \langle e|$. This means that any gate which takes a finite time will result in some non-vanishing qubit/cavity entanglement. We wish to characterize and minimize these errors for the respective Hilbert space size we access.

We can rewrite Eq. S12 in terms of Pauli spin operators σ_z and σ_y

$$\tilde{H}/\hbar = \sum_n \{-\chi_{qs}(n-m)\frac{\sigma_z}{2} + \epsilon(t)\sigma_y\} \, |n\rangle \langle n| \, . \qquad \text{(S19)}$$

This interaction occurs with a constant drive amplitude ϵ for a time τ resulting in a block diagonal evolution operator

$$\begin{aligned} U(\tau) &= e^{-i\tilde{H}/\hbar\tau} \\ &= \sum_n U_n(\tau) \, |n\rangle \langle n| \\ &= \sum_n e^{-i\tau\{\chi_{qs}(m-n)\frac{\sigma_z}{2} + \epsilon\sigma_y\}} \, |n\rangle \langle n| \\ &= \sum_n e^{-i\phi_n \sigma_{\theta_n}} \, |n\rangle \langle n| \end{aligned} \qquad \text{(S20)}$$

where $\phi_n = \epsilon\tau\sqrt{1 + \left[\frac{(m-n)\chi_{qs}}{2\epsilon}\right]^2}$, $\theta_n = \arctan\left(\frac{(m-n)\chi_{qs}}{2\epsilon}\right)$, and $\sigma_{\theta_n} = \cos(\theta_n)\sigma_y + \sin(\theta_n)\sigma_z$. This allows us to write each photon-dependent operation explicitly as

$$\begin{aligned} U_n(\tau) &= e^{-i\phi_n\sigma_{\theta_n}} \\ &= \cos(\phi_n)\mathbb{1} + i\sin(\phi_n)\sigma_{\theta_n} \\ &= [\cos(\phi_n) + i\sin(\phi_n)]\sin(\theta_n) \, |n,g\rangle \langle n,g| \\ &\quad + [\cos(\phi_n) - i\sin(\phi_n)]\sin(\theta_n) \, |n,e\rangle \langle n,e| \\ &\quad + \sin(\phi_n)\cos(\theta_n)(|n,e\rangle \langle n,g| - |n,g\rangle \langle n,e|). \end{aligned} \qquad \text{(S21)}$$

Using this relation, we can estimate this operation's ability to be independent of all photon number states in a defined cavity Hilbert space size. For our experiment, we apply an unconditional qubit $\pi/2$ rotation using a square pulse for time $\tau = 4$ ns. We can compare this operation to an ideal unconditional qubit rotation $R_{\hat{y},\frac{\pi}{2}}$ to get an estimated gate fidelity $\mathcal{F} = |\frac{1}{N}\mathrm{Tr}[R^\dagger_{\hat{y},\frac{\pi}{2}} U(\tau)]|^2$ greater than 0.96 for a Hilbert space size $N = 20$ photons (this is the approximate Hilbert space size of the measured cat in Fig. 2 of the main text). This operation will become increasingly ineffective for large numbers of photons which is a leading cause for infidelities in Wigner tomography. This can be corrected somewhat by moving the qubit drive to a frequency $\omega_q^m = \omega_q - \bar{n}\chi_{qs}$ for a cavity state with mean photon number $\bar{n}$. This procedure was required in order to measure our largest produced cat state.

Conditional cavity displacements

The cavity transition frequency is dependent on the qubit state resulting in two spectral peaks ω_s^g and ω_s^e representing the cavity transition frequency when the qubit is in the $|g\rangle$ and $|e\rangle$ state respectively. Using Eq. 1 of the main text, we can introduce a classical drive on resonance with the ω_s^e transition resulting in the Hamiltonian (in the rotating frame of the drive)

$$\begin{aligned} H_{\mathrm{drive}}/\hbar = (\omega_q - \omega_s^e) \, |e\rangle \langle e| - \chi_{qs} \, |g\rangle \langle g| \, a^\dagger a \\ + \; \epsilon(t)a^\dagger + \epsilon(t)^* a. \end{aligned}$$

In the same manner as the conditional qubit rotation, a cavity drive with a small spectral width $\sigma_\omega \ll \chi_{qs}$ will be able to selectively drive a displacement D_α conditioned on the qubit in the excited state $|e\rangle$. This results in the approximate qubit/cavity entangling operation

$$D_\alpha^e = \; \mathbb{1} \otimes e^{i\xi} \, |g\rangle \langle g| + D_\alpha \otimes |e\rangle \langle e| \qquad \text{(S22)}$$

where ξ is an induced phase accumulated on $|g\rangle$ due to the AC stark effect. For example, the conditional cavity displacement D_α^e acting on a qubit/cavity product state produces $D_\alpha^e\{|0\rangle \otimes (|g\rangle + |e\rangle)\} = e^{i\xi} \, |0,g\rangle + |\alpha,e\rangle$ resulting in an entangled qubit/cavity state. This entangling operation could be used directly in the mapping sequence, but in practice is ineffective due to its long required gate time. Though we do not use this operation in our mapping sequence we do use this feature for experiment initialization (see section, 'Experiment initialization'). A selective displacement D_α^e can also be achieved by combining a conditional cavity phase shift C_π with ordinary cavity displacements: $D_\alpha^e = D_{-\alpha/2} C_\pi D_{\alpha/2}$.

Unconditional cavity displacements

We must also ensure that our standard cavity displacements D_α will displace the cavity state unconditional of the qubit state. Unconditional cavity displacements are used throughout for qubit/cavity mapping and for Wigner tomography. For our cavity displacements, we apply a square-shaped displacement pulse $U(\tau)$ where $\tau = 6$ ns which we estimate a gate fidelity due to finite pulse width $\mathcal{F} = |\frac{1}{N}\,\mathrm{Tr}[D_\alpha^\dagger U(\tau)]|^2 > 0.99$.

SUPPLEMENTARY FIGURES

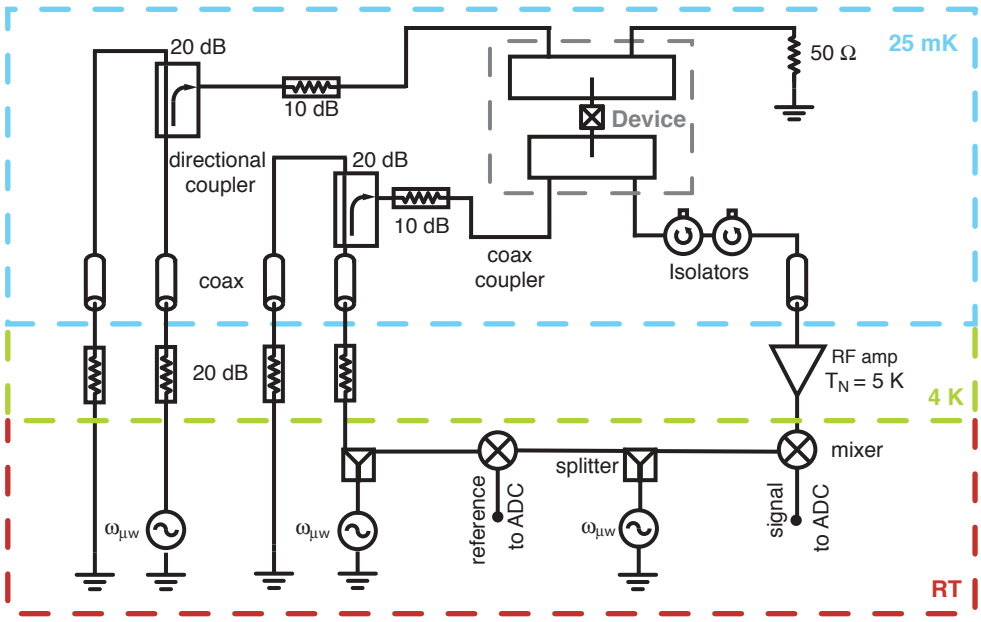

FIG. S1. **Block diagram of the measurement setup**. We use two input lines, one directed into the readout (high-frequency cavity) mode and another into the storage (low-frequency cavity) mode. Qubit state manipulations are controlled through this 'low-frequency' input line. Our readout signal is sent through a chain of amplifiers before down-conversion and finally digitization.

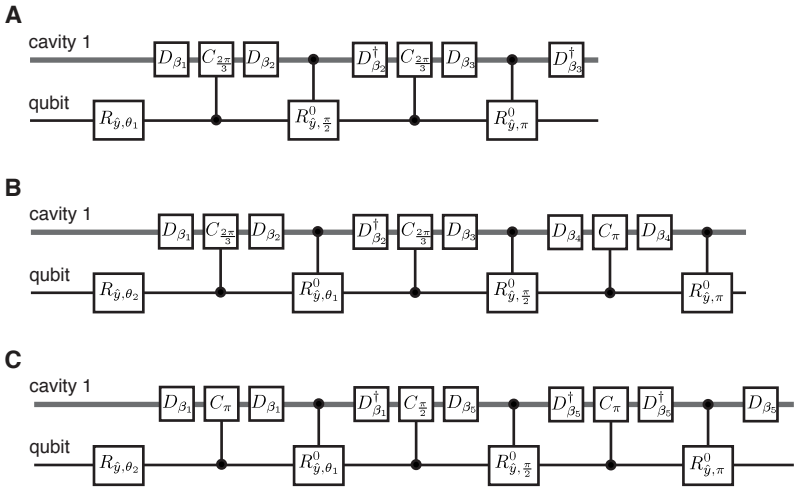

FIG. S2. **Multi-component cat state sequences**. Each quantum circuit diagram (**A**, **B**, **C**) describes the pulse sequences used to create the cavity states shown in Fig. 4(**A**, **B**, **C**). β_1, β_2, β_3, β_4, and β_5 equals $|\beta|$, $|\beta|e^{-i\frac{\pi}{3}}$, $|\beta|e^{i\frac{\pi}{3}}$, $\frac{|\beta|}{2}e^{-i\frac{2\pi}{3}}$, and $|\beta|e^{i\frac{\pi}{2}}$ respectively with $|\beta| = \sqrt{7}$ and θ_1, θ_2 equals $2\arccos\frac{1}{\sqrt{3}}$, $2\arccos\frac{1}{2}$ respectively. Note that the phase of each selective drive $R^0_{\hat{n},\theta}$ will determine the phase of the interference fringes between the produced superpositions of coherent states.

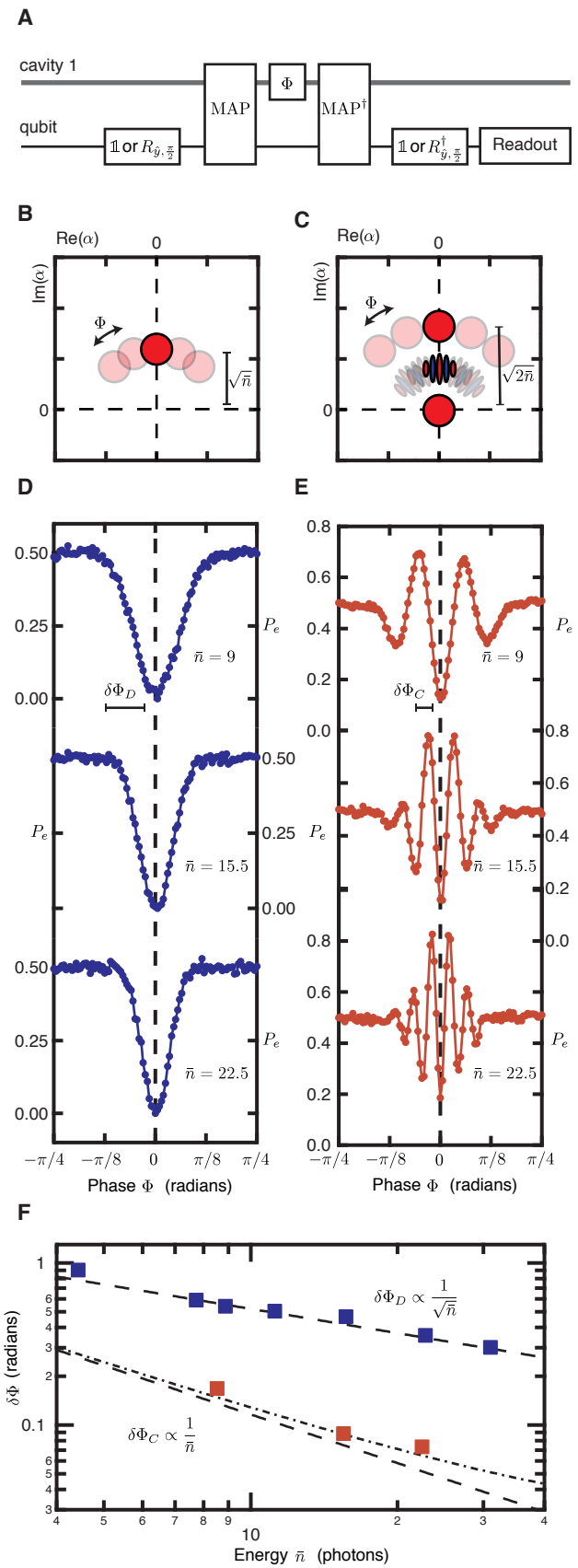

FIG. S3. **Heisenberg-limited phase estimation**. (**A**) The circuit diagram outlines the methods to perform a proof-of-principle Heisenberg-limited phase estimation. In two different experiments, we create coherent states or cat states and compare phase resolution $\delta\Phi$ to each state's mean energy $\bar{n}$. (**B,C**) To do this, we implement a cavity phase shift Φ on each prepared cavity state before reversing the mapping process. We measure the resulting qubit state population P_e for coherent states (**D**) and cat states (**E**) with various mean energies. (**F**) Using these measurements, we can observe the phase resolution for a coherent state (■) and a cat state (■) to scale as $1/\sqrt{\bar{n}}$ and $1/\bar{n}$, respectively, demonstrating a proof-of-principle for Heisenberg-limited phase estimation using cat states. Note that in practice a cat state is increasingly sensitive to photon decay at larger energies. This gives a phase resolution $\delta\Phi_C \propto e^{\bar{n}\kappa\tau}/\bar{n}$ where κ is the cavity decay rate and τ is the total time of state preparation and phase detection (shown in **F**: - - -), which will become unfavorable when $\bar{n}\kappa\tau > 1$.

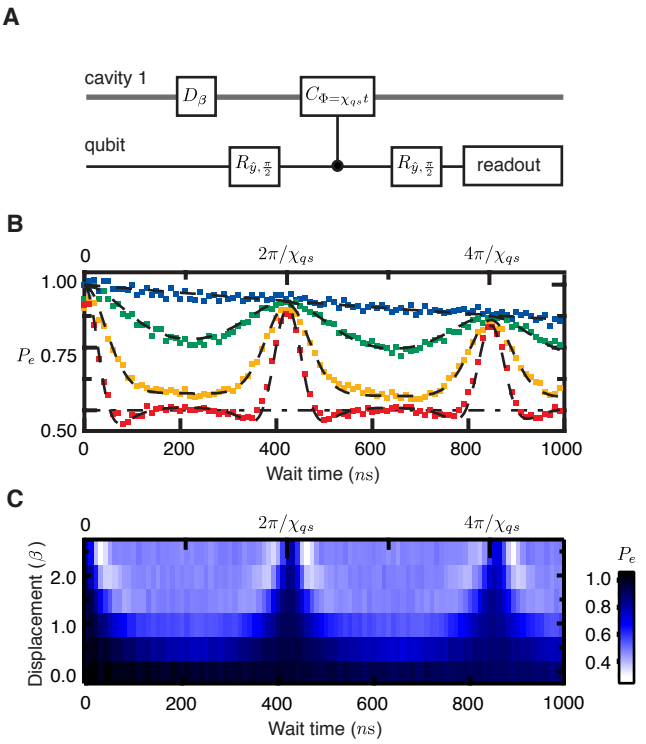

FIG. S4. **Qubit state revival using Ramsey interferometry**. A quantum circuit (**A**) outlines the sequence for Ramsey interferometry of a coherent state under a dispersive interaction. An initial state $\psi(0) = |\beta\rangle \otimes \{|g\rangle + |e\rangle\}$ is prepared and precesses under the operation, $C_{\Phi=\chi_{qs}t} = e^{i\chi_{qs}a^\dagger a|e\rangle\langle e|}$. We perform this measurement for various displacement amplitudes (**B**: $\beta = 0$ ■, 0.5 ■, 1.0 ■, and 1.5 ■). Qubit state coherence appears to decay due to this interaction at a rate proportional to $e^{-\frac{1}{2}(|\beta|\chi_{qs}t)^2}$. Qubit state revival occurs at a waiting time $t_{\text{revival}} = 2\pi/\chi$. Notice the width in the revival peak sharply decreases with larger displacement amplitudes (**C**).

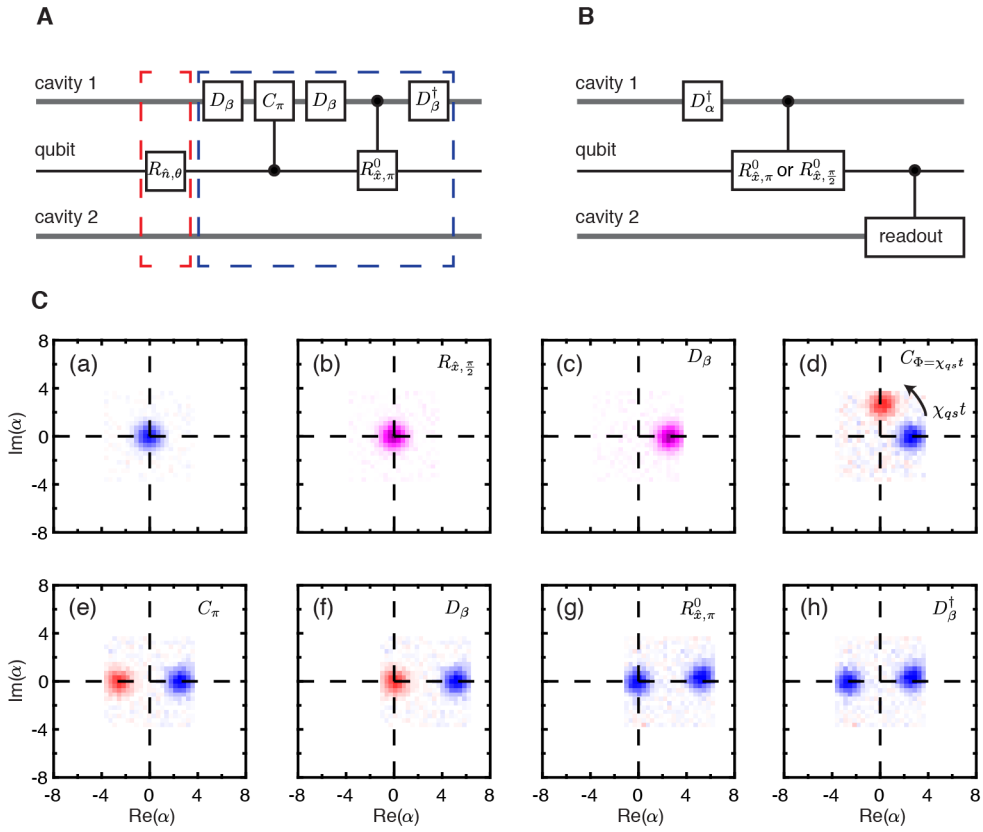

FIG. S5. **Observing each step of the qcMAP**. Measuring qubit/cavity correlated Q-functions shows the cavity state phase and amplitude throughout each step in the mapping protocol (**A**). Cavity tomography is performed with a 21 X 21 grid of displacements using a span of 8α in both quadratures (**B**). By performing a selective π or $\pi/2$ rotation conditioned on the zero-photon Fock state, we can detect Q-functions correlated to the qubit state. $Q(\alpha)_{|g\rangle}$ (■) corresponds to cavity state population with the qubit in $|g\rangle$, $Q(\alpha)_{|e\rangle}$ (■) corresponds to cavity state population with the qubit in $|e\rangle$, and $Q(\alpha)_{|g\rangle+|e\rangle}$ (■) corresponds to cavity state population with the qubit in $|g\rangle + |e\rangle$. This allows us to observe qubit/cavity states during each step (**C**[a-h]) and ultimately calibrate the qcMAP protocol.

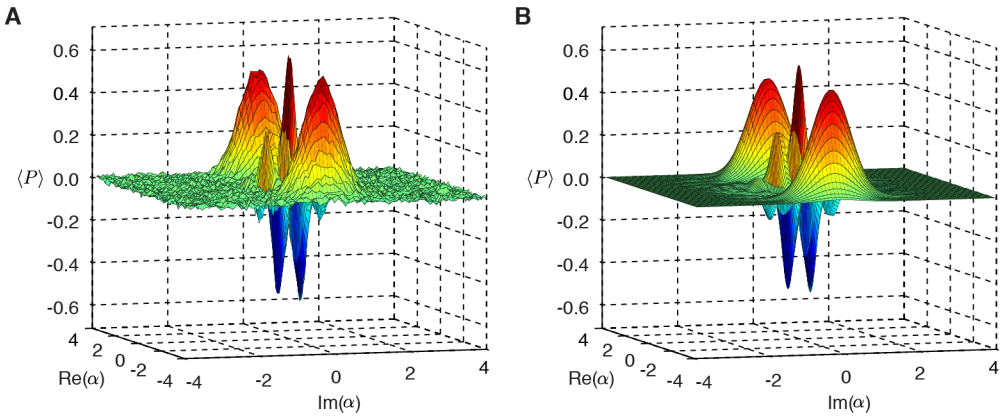

FIG. S6. **Measured and reconstructed cavity state Wigner function**. Direct measurement (**A**) and reconstruction (**B**) of the cavity state Wigner function for a state $|\psi\rangle = \mathcal{N}\{|\beta\rangle + |-\beta\rangle\}$ where $|\beta| = \sqrt{7}$ and $\mathcal{N} \approx \frac{1}{\sqrt{2}}$. Mean values for cavity state observables can be calculated both from the direct Wigner measurement and from the reconstructed cavity state density matrix.

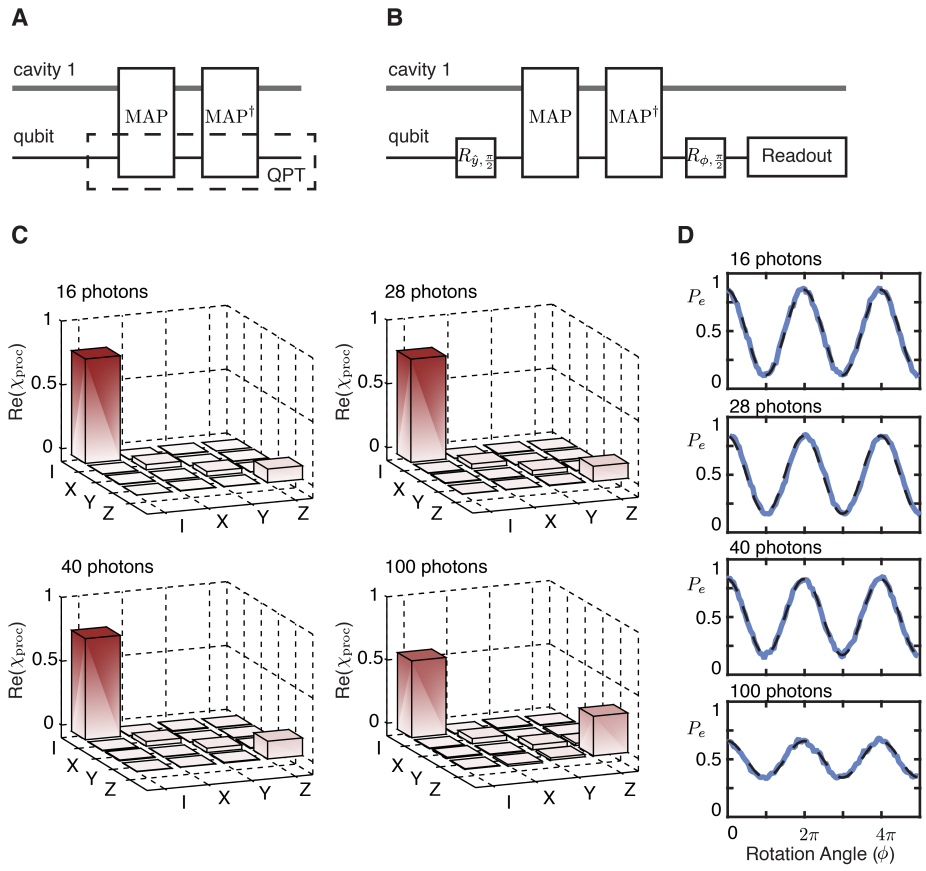

FIG. S7. **Write/Read analysis of qcMAP**. In order to diagnose possible qcMAP errors, we perform both quantum process tomography and Ramsey experiments on the map/map-back operation. Quantum process tomography (**A, C**) of the map/map-back operation on the qubit reveals increased phase errors at larger photon numbers (note: all imaginary portions of the process matrix are $< |0.06|$). This suggests that phase coherence is a dominant source of error in the mapping operation and that this error is increasingly sensitive to photon loss in the cavity. This Ramsey experiment (**B, D**) shows a recovered contrast in qubit coherence of 74, 68, 67, and 31% for cat states with estimated sizes up to 100 photons.

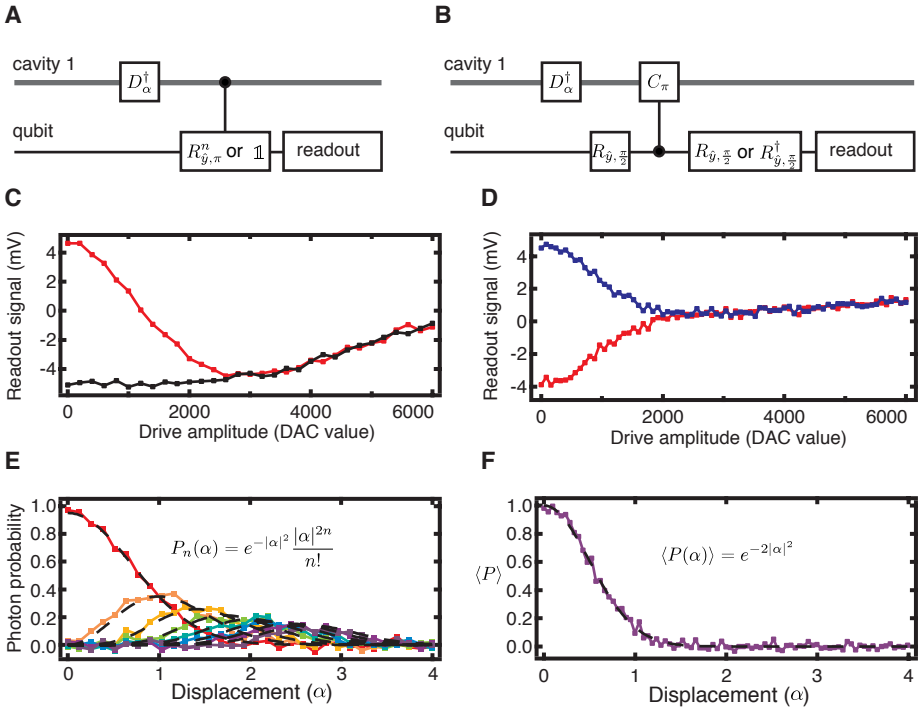

FIG. S8. **Calibrating displacement amplitude and removing cross-Kerr readout skewness** Using conditional qubit rotations $R^0_{\hat{n},\pi}$or conditional cavity phase shifts C_π, we can measure the photon number probability P_n or the mean photon parity $\langle P\rangle$ of the cavity state. Shown here (**A**, **B**), are the circuit diagrams for detecting P_n and $\langle P\rangle$, respectively, as a function of α. Residual cavity-cavity cross-talk (also known as the Cross-Kerr χ_{sr}) will skew the readout signal for large displacements. This background signal can be corrected by comparing to an additional experiment which is qubit state-independent. Shown (**C**) is the uncorrected signal for detecting P_0 (■) after various displacements and its corresponding 'correction' experiment (■). Shown in (**D**) is the uncorrected signal for detecting $\langle P\rangle$ (■) of various displacements and its corresponding 'correction' experiment (■). From these measurements, we can deduce P_n (**E**: $n = 0$ ■, 1 ■, 2 ■, 3 ■, 4 ■, 5 ■, 6 ■, 7 ■ photons) and $\langle P\rangle$ (**F**: ■)of a displaced vacuum state. Note that these measurements for P_0 and $\langle P\rangle$ are measurements of cuts in the cavity Q-function and Wigner function of a vacuum state.

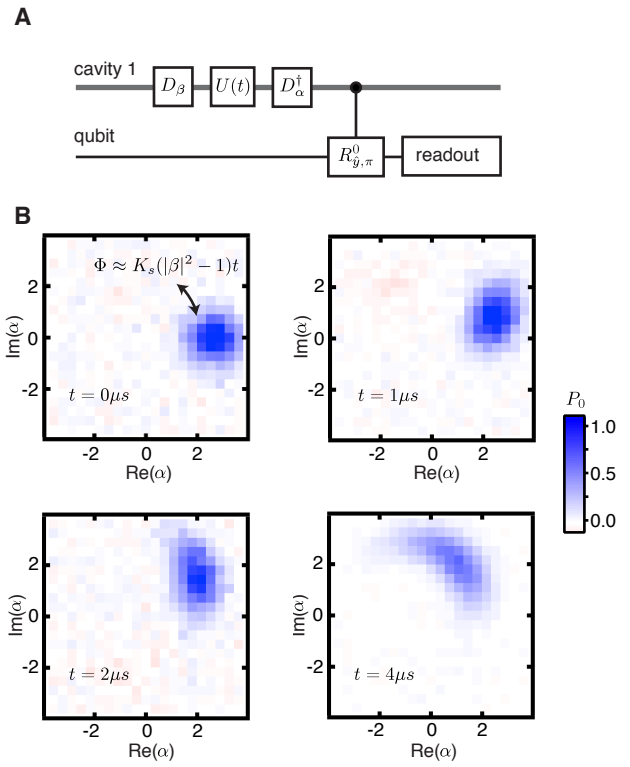

FIG. S9. **Observing the cavity self-Kerr**. The cavity Hamiltonian obtains some non-linearity known as the cavity self-Kerr $K_s a^{\dagger 2} a^2$ by its off-resonant coupling to the qubit mode. This interaction will induce a photon-dependent phase precession. We observe this interaction by creating a coherent state, allowing the state to evolve under $U(t) = e^{iK_s a^{\dagger 2} a^2 t}$, then subsequently measure the cavity Q-function (**A**). For a coherent state $|\beta\rangle$ where $|\beta| = \sqrt{7}$, we observe a coherent state precession and phase-collapse for waiting times $t = 0$, 1, 2, and $4\mu s$ (**B**). We detect a self-Kerr $\frac{K_s}{2\pi} = 3.61$ kHz by performing a global fit to all Q-function with displacement amplitude $|\beta|$, initial cavity phase Φ_0, and cavity self-Kerr K_s as fit parameters. This results in a ratio K_s/χ_{qs} of 0.0014. Notice the increasing angular spread of the coherent state as waiting time increases, a feature inherent under a Kerr interaction and a source for qcMAP infidelity.

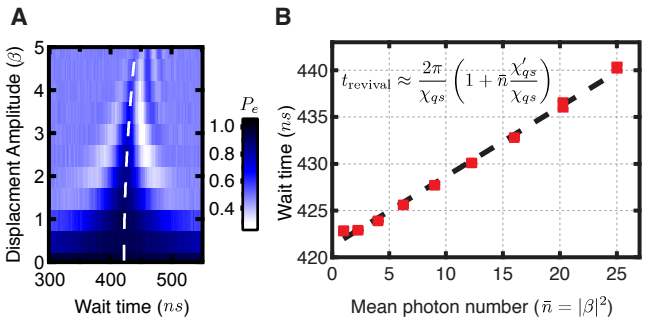

FIG. S10. **Observing the non-linearity of the dispersive shift**. We perform Ramsey interferometry (see Fig. S4) and observe the qubit state revival for displacements up to $|\beta| = 5$ (**A**). These measurements reveal the skewness in revival time due to a small photon dependence of the dispersive shift, $\chi'_{qs}a^{\dagger 2}a^2$. Taking this shift in revival time into account gives $t_{\text{revival}} \approx \frac{2\pi}{\chi_{qs}-|\beta|^2\chi'_{qs}}$. For small ratios $\bar{n}\chi'_{qs}/\chi_{qs} \ll 1$ where $\bar{n} = |\beta|^2$, this follows the linear relationship $t_{\text{revival}} \approx \frac{2\pi}{\chi_{qs}}(1 + \bar{n}\chi'_{qs}/\chi_{qs})$ which allows us to measure a ratio $\chi'_{qs}/\chi_{qs} = 0.0018$ resulting in a $\frac{\chi'_{qs}}{2\pi} = 4.2$ kHz (**B**).

SUPPLEMENTARY TABLES

TABLE SI. **Hamiltonian parameters**. Using a normal state resistance measurement to determine the Josephson energy E_J and experimental measurements of K_q, χ_{qs}, and χ_{qr} to determine each mode's flux coefficient ϕ_i, we can predict the values of higher-order interactions in this three-mode Hamiltonian. These estimates comes from the Taylor expansion of the $\cos\varphi$ term in Eq. 19 and collecting all terms in a normal order. This table shows the measured or predicted value of each term in the Hamiltonian (Eq. 21) up to $\mathcal{O}(\varphi^6)$.

Order	Term	Relation	Measurement	Prediction
	$\omega_q/2\pi$	-	7.4552 GHz	-
-	$\omega_s/2\pi$	-	8.1794 GHz	-
	$\omega_r/2\pi$	-	9.3622 GHz	-
	$K_q/2\pi$		133.5 MHz	-
$\mathcal{O}(\varphi^4)$	$K_s/2\pi$	$\frac{1}{4!}\binom{4}{2}\binom{2}{2}E_J\phi_i^4$	3.6 kHz	2.7 ± 0.4 kHz
	$K_r/2\pi$		-	2.7 ± 0.4 kHz
	$\chi_{qs}/2\pi$		2.36 MHz	-
$\mathcal{O}(\varphi^4)$	$\chi_{qr}/2\pi$	$\frac{1}{4!}\binom{4}{1}\binom{3}{1}\binom{2}{1}\binom{1}{1}E_J\phi_i^2\phi_j^2$	2.40 MHz	-
	$\chi_{rs}/2\pi$		-	2.7 ± 0.3 kHz
	$K_q'/2\pi$		-	6 ± 1 MHz
$\mathcal{O}(\varphi^6)$	$K_s'/2\pi$	$\frac{1}{6!}\binom{6}{3}\binom{3}{3}E_J\phi_i^6$	-	600 ± 100 mHz
	$K_r'/2\pi$		-	500 ± 100 mHz
	$\chi_{qs}'/2\pi$		4.2 kHz	0.4 ± 0.1 kHz
	$\chi_{qr}'/2\pi$		-	400 ± 100 Hz
$\mathcal{O}(\varphi^6)$	$\chi_{sq}'/2\pi$	$\frac{1}{6!}\binom{6}{2}\binom{4}{2}\binom{2}{1}\binom{1}{1}E_J\phi_i^2\phi_j^4$	-	80 ± 10 kHz
	$\chi_{rq}'/2\pi$		-	80 ± 10 kHz
	$\chi_{rs}'/2\pi$		-	1.7 ± 0.3 Hz
	$\chi_{sr}'/2\pi$		-	1.6 ± 0.3 Hz
$\mathcal{O}(\varphi^6)$	$\chi_{qsr}/2\pi$	$\frac{1}{6!}\binom{6}{1}\binom{5}{1}\binom{4}{1}\binom{3}{1}\binom{2}{1}\binom{1}{1}E_J\phi_i^2\phi_j^2\phi_k^2$	-	370 ± 50 mHz

TABLE SII. **Inferred expectation values of observables** Shown are operators, $O(a^\dagger a)$ and their corresponding complex functions, $o(\alpha^*, \alpha)$ with inferred expectation values of photon number $a^\dagger a$, position $\frac{1}{2}(a^\dagger + a)$, momentum $\frac{1}{2i}(a^\dagger - a)$, and fidelity to a target state $\langle\psi_{\rm targ}|\hat{\rho}|\psi_{\rm targ}\rangle$ where $|\psi_{\rm targ}\rangle = \mathcal{N}(|\beta\rangle + |-\beta\rangle)$ and $|\beta| = \sqrt{7}$.

Operator	Complex Function	Expection value	
$O(a^\dagger, a)$	$o(\alpha^*, \alpha)$	$\mathrm{Tr}[O\rho]$	$\frac{1}{\pi}\int oW\mathrm{d}^2\alpha$
$a^\dagger a$	$\alpha^*\alpha - \frac{1}{2}$	6.79	6.65
$\frac{1}{2}(a^\dagger + a)$	$\frac{1}{2}(\alpha^* + \alpha)$	0.09	0.13
$\frac{1}{2i}(a^\dagger - a)$	$\frac{1}{2i}(\alpha^* - \alpha)$	−0.01	−0.01
$\|\psi_{\rm targ}\rangle\langle\psi_{\rm targ}\|$	$W_{\rm targ}(\alpha^*, \alpha)$	0.78	0.81

References and Notes

1. J. M. Raimond, T. Meunier, P. Bertet, S. Gleyzes, P. Maioli, A. Auffeves, G. Nogues, M. Brune, S. Haroche, Probing a quantum field in a photon box. *J. Phys. B* **38**, S535–S550 (2005). doi:10.1088/0953-4075/38/9/006

2. R. Miller, T. E. Northup, K. M. Birnbaum, A. Boca, A. D. Boozer, H. J. Kimble, Trapped atoms in cavity QED: Coupling quantized light and matter. *J. Phys. B* **38**, S551–S565 (2005). doi:10.1088/0953-4075/38/9/007

3. A. Wallraff, D. I. Schuster, A. Blais, L. Frunzio, R. Huang, J. Majer, S. Kumar, S. M. Girvin, R. J. Schoelkopf, Strong coupling of a single photon to a superconducting qubit using circuit quantum electrodynamics. *Nature* **431**, 162–167 (2004). Medline doi:10.1038/nature02851

4. L. DiCarlo, J. M. Chow, J. M. Gambetta, L. S. Bishop, B. R. Johnson, D. I. Schuster, J. Majer, A. Blais, L. Frunzio, S. M. Girvin, R. J. Schoelkopf, Demonstration of two-qubit algorithms with a superconducting quantum processor. *Nature* **460**, 240–244 (2009). Medline doi:10.1038/nature08121

5. R. Vijay, D. H. Slichter, I. Siddiqi, Observation of quantum jumps in a superconducting artificial atom. *Phys. Rev. Lett.* **106**, 110502 (2011). Medline doi:10.1103/PhysRevLett.106.110502

6. M. Hatridge, S. Shankar, M. Mirrahimi, F. Schackert, K. Geerlings, T. Brecht, K. M. Sliwa, B. Abdo, L. Frunzio, S. M. Girvin, R. J. Schoelkopf, M. H. Devoret, Quantum back-action of an individual variable-strength measurement. *Science* **339**, 178–181 (2013). Medline doi:10.1126/science.1226897

7. A. A. Houck, D. I. Schuster, J. M. Gambetta, J. A. Schreier, B. R. Johnson, J. M. Chow, L. Frunzio, J. Majer, M. H. Devoret, S. M. Girvin, R. J. Schoelkopf, Generating single microwave photons in a circuit. *Nature* **449**, 328–331 (2007). Medline doi:10.1038/nature06126

8. C. Eichler, C. Lang, J. M. Fink, J. Govenius, S. Filipp, A. Wallraff, Observation of entanglement between itinerant microwave photons and a superconducting qubit. *Phys. Rev. Lett.* **109**, 240501 (2012). Medline doi:10.1103/PhysRevLett.109.240501

9. P. J. Leek, M. Baur, J. M. Fink, R. Bianchetti, L. Steffen, S. Filipp, A. Wallraff, Cavity quantum electrodynamics with separate photon storage and qubit readout modes. *Phys. Rev. Lett.* **104**, 100504 (2010). Medline doi:10.1103/PhysRevLett.104.100504

10. M. Mariantoni, H. Wang, R. C. Bialczak, M. Lenander, E. Lucero, M. Neeley, A. D. O'Connell, D. Sank, M. Weides, J. Wenner, T. Yamamoto, Y. Yin, J. Zhao, J. M. Martinis, A. N. Cleland, Photon shell game in three-resonator circuit quantum electrodynamics. *Nat. Phys.* **7**, 287–293 (2011). doi:10.1038/nphys1885

11. D. Gottesman, A. Kitaev, J. Preskill, Encoding a qubit in an oscillator. *Phys. Rev. A* **64**, 012310 (2001). doi:10.1103/PhysRevA.64.012310

12. Z. Leghtas *et al*., arXiv: 1207.0679.

13. M. Hofheinz, H. Wang, M. Ansmann, R. C. Bialczak, E. Lucero, M. Neeley, A. D. O'Connell, D. Sank, J. Wenner, J. M. Martinis, A. N. Cleland, Synthesizing arbitrary quantum states in a superconducting resonator. *Nature* **459**, 546–549 (2009). Medline doi:10.1038/nature08005

14. B. R. Johnson, M. D. Reed, A. A. Houck, D. I. Schuster, L. S. Bishop, E. Ginossar, J. M. Gambetta, L. DiCarlo, L. Frunzio, S. M. Girvin, R. J. Schoelkopf, Quantum non-demolition detection of single microwave photons in a circuit. *Nat. Phys.* **6**, 663–667 (2010). doi:10.1038/nphys1710

15. M. Brune, E. Hagley, J. Dreyer, X. Maître, A. Maali, C. Wunderlich, J. M. Raimond, S. Haroche, Observing the Progressive Decoherence of the "Meter" in a Quantum Measurement. *Phys. Rev. Lett.* **77**, 4887–4890 (1996). Medline doi:10.1103/PhysRevLett.77.4887

16. G. Kirchmair, B. Vlastakis, Z. Leghtas, S. E. Nigg, H. Paik, E. Ginossar, M. Mirrahimi, L. Frunzio, S. M. Girvin, R. J. Schoelkopf, Observation of quantum state collapse and revival due to the single-photon Kerr effect. *Nature* **495**, 205–209 (2013). Medline doi:10.1038/nature11902

17. L. Lutterbach, L. Davidovich, Method for Direct Measurement of the Wigner Function in Cavity QED and Ion Traps. *Phys. Rev. Lett.* **78**, 2547–2550 (1997). doi:10.1103/PhysRevLett.78.2547

18. Z. Leghtas, G. Kirchmair, B. Vlastakis, M. H. Devoret, R. J. Schoelkopf, M. Mirrahimi, Deterministic protocol for mapping a qubit to coherent state superpositions in a cavity. *Phys. Rev. A* **87**, 042315 (2013). doi:10.1103/PhysRevA.87.042315

19. W. H. Zurek, Sub-Planck structure in phase space and its relevance for quantum decoherence. *Nature* **412**, 712–717 (2001). Medline doi:10.1038/35089017

20. C. M. Caves, A. Shaji, Quantum-circuit guide to optical and atomic interferometry. *Opt. Commun.* **283**, 695–712 (2010). doi:10.1016/j.optcom.2009.10.065

21. S. Deléglise, I. Dotsenko, C. Sayrin, J. Bernu, M. Brune, J. M. Raimond, S. Haroche, Reconstruction of non-classical cavity field states with snapshots of their decoherence. *Nature* **455**, 510–514 (2008). Medline doi:10.1038/nature07288

22. A. Ourjoumtsev, H. Jeong, R. Tualle-Brouri, P. Grangier, Generation of optical 'Schrödinger cats' from photon number states. *Nature* **448**, 784–786 (2007). Medline doi:10.1038/nature06054

23. P. Bertet, A. Auffeves, P. Maioli, S. Osnaghi, T. Meunier, M. Brune, J. M. Raimond, S. Haroche, Direct measurement of the Wigner function of a one-photon Fock state in a cavity. *Phys. Rev. Lett.* **89**, 200402 (2002). Medline doi:10.1103/PhysRevLett.89.200402

24. See accompanying supplementary materials for details.

25. M. Boissonneault, J. M. Gambetta, A. Blais, Dispersive regime of circuit QED: Photon-dependent qubit dephasing and relaxation rates. *Phys. Rev. A* **79**, 013819 (2009). doi:10.1103/PhysRevA.79.013819

26. H. Paik, D. I. Schuster, L. S. Bishop, G. Kirchmair, G. Catelani, A. P. Sears, B. R. Johnson, M. J. Reagor, L. Frunzio, L. I. Glazman, S. M. Girvin, M. H. Devoret, R. J. Schoelkopf, Observation of high coherence in Josephson junction qubits measured in a three-dimensional circuit QED architecture. *Phys. Rev. Lett.* **107**, 240501 (2011). Medline doi:10.1103/PhysRevLett.107.240501

27. C. Monroe, D. M. Meekhof, B. E. King, D. J. Wineland, A "Schrodinger Cat" Superposition State of an Atom. *Science* **272**, 1131–1136 (1996). Medline doi:10.1126/science.272.5265.1131

28. D. I. Schuster, A. A. Houck, J. A. Schreier, A. Wallraff, J. M. Gambetta, A. Blais, L. Frunzio, J. Majer, B. Johnson, M. H. Devoret, S. M. Girvin, R. J. Schoelkopf, Resolving photon number states in a superconducting circuit. *Nature* **445**, 515–518 (2007). Medline doi:10.1038/nature05461

29. S. Haroche, J. M. Raimond, *Exploring the Quantum: Atoms, Cavities, and Photons* (Oxford Univ. Press, 2006).

30. S. L. Braunstein, P. van Loock, Quantum information with continuous variables. *Rev. Mod. Phys.* **77**, 513–577 (2005). doi:10.1103/RevModPhys.77.513

31. S. E. Nigg, S. M. Girvin, Stabilizer Quantum Error Correction Toolbox for Superconducting Qubits. *Phys. Rev. Lett.* **110**, 243604 (2013). doi:10.1103/PhysRevLett.110.243604

32. H. Jeong, T. Ralph, Quantum superpositions and entanglement of thermal states at high temperatures and their applications to quantum-information processing. *Phys. Rev. A* **76**, 042103 (2007). doi:10.1103/PhysRevA.76.042103

33. S. E. Nigg, H. Paik, B. Vlastakis, G. Kirchmair, S. Shankar, L. Frunzio, M. H. Devoret, R. J. Schoelkopf, S. M. Girvin, Black-box superconducting circuit quantization. *Phys. Rev. Lett.* **108**, 240502 (2012). Medline doi:10.1103/PhysRevLett.108.240502

34. C. Hempel, B. P. Lanyon, P. Jurcevic, R. Gerritsma, R. Blatt, C. F. Roos, Entanglement-enhanced detection of single-photon scattering events. *Nat. Photonics* **7**, 630–633 (2013). doi:10.1038/nphoton.2013.172

35. M. P. da Silva, O. Landon-Cardinal, D. Poulin, Practical characterization of quantum devices without tomography. *Phys. Rev. Lett.* **107**, 210404 (2011). Medline doi:10.1103/PhysRevLett.107.210404

36. K. Cahill, R. Glauber, *Phys. Rev.* **177**, 5 (1969).

37. M. O. Scully, M. S. Zubairy, *Quantum Optics* (Cambridge Univ. Press, 2013).